


Patterns, spin-spin correlations, and competing instabilities in driven quasi-two-dimensional spin-1 Bose-Einstein condensates

Sandra M. Jose ¹, Komal Sah ^{1,2} and Rejish Nath ¹

¹*Department of Physics, Indian Institute of Science Education and Research, Pune 411 008, India*

²*Department of Physics, University of California, Davis, California 95616, USA*

 (Received 21 May 2023; accepted 31 July 2023; published 11 August 2023; corrected 28 August 2024)

We analyze the formation of transient patterns and spin-spin correlations in quasi-two-dimensional spin-1 homogeneous Bose-Einstein condensates subjected to parametric driving of s -wave scattering lengths. The dynamics for an initial ferromagnetic phase is identical to that of a scalar condensate. In contrast, intriguing dynamics emerges for an initial polar state. For instance, we show that competition exists between density patterns and spin-mixing dynamics. Dominant spin-mixing dynamics lead to a gas of polar core vortices and antivortices of different spin textures. The density modes of the Bogoliubov spectrum govern the wave-number selection of Faraday patterns. The spin modes determine the vortex density and the spatial dependence of spin-spin correlation functions. When the density patterns outgrow the spin-mixing dynamics, the spin-spin correlations decay exponentially with a correlation length of the order of a spin healing length; otherwise, they exhibit a Bessel function dependence. Strikingly, competing instabilities within density and spin modes emerge when both scattering lengths are modulated at different frequencies and appropriate modulation amplitudes. The competing instability leads to a superposition of density patterns or correlation functions of two distinct wavelengths. Our studies reveal that fine control over the driven dynamics can be attained by tuning interaction strengths, quadratic Zeeman field, driving frequencies, and amplitudes.

DOI: [10.1103/PhysRevA.108.023308](https://doi.org/10.1103/PhysRevA.108.023308)

I. INTRODUCTION

Periodically driven Bose-Einstein condensates have been a playground for studying various phenomena such as Faraday patterns [1–17], dark-soliton lattices [18], dynamical localization [19–21], spin freezing [22,23], matter-wave jets [24–27], bright solitons [28,29], parametric instability [30], the generation of higher harmonics [31], etc. Faraday patterns are observed experimentally in elongated condensates by modulating either the trap frequencies [2,16] or the interactions [32,33]. Such patterns offer critical insights into the elementary excitations of condensates because the pattern size is determined by the Bogoliubov mode resonant with half of the driving frequency. A nonmonotonous excitation spectrum can make the wave-number selection nontrivial [4,10].

Because of the spin degrees of freedom, spinor condensates are ideal for exploring spin textures and magnetic phases [34–36]. Interesting phenomena such as dynamical stabilization [23], spin squeezing [37,38], Shapiro resonances [39,40], parametric resonances [41], and the quantum walk in momentum space [42,43] have been reported in driven spinor condensates. In this paper, we analyze the formation of transient density and spin patterns and spin-spin correlations in a quasi-two-dimensional (Q2D) spin-1 homogeneous condensate subjected to the parametric driving of s -wave scattering lengths a_0 and a_2 . We consider three cases where either a_0 or a_2 is modulated individually or both are modulated simultaneously. Modulating either a_0 or a_2 leads to modulations in both spin-independent and spin-dependent interactions, affecting the dynamics of both spatial and spin degrees of freedom.

As we show, the dynamics depends critically on the initial states, and in particular, we consider ferromagnetic and polar phases. A ferromagnetic phase is immune to the modulation of a_0 [44], whereas a_2 modulation results in dynamics similar to that of a driven scalar condensate [1,2]. In contrast, an initial polar condensate exhibits nontrivial dynamics. Unstable Bogoliubov modes lead to both Faraday patterns and spin-mixing dynamics. There exists an implicit competition between density modulations and spin-mixing dynamics. When the spin mixing becomes dominant, a gas of polar core vortices (PCVs) and antivortices of different spin textures are formed. Previous studies on PCVs in Q2D spin-1 condensates were based on the Kibble-Zurek mechanism via quenching of the quadratic Zeeman field from nonpolar phases [37,45,46]. The unstable momentum of the density mode quantifies the wave number of the Faraday pattern, whereas that of the spin mode determines the vortex density. At longer times, spin mixing disrupts the selection of higher harmonics, which is highly in contrast to the case of a scalar condensate. If the spin-dependent interactions are stronger than the spin-independent ones, the Faraday patterns outgrow the spin dynamics, and the spin-spin correlations decay exponentially over distance with a correlation length of the order of a spin healing length. In contrast, when the spin dynamics are dominant, the spin-spin correlations are governed by a Bessel function with an argument depending on the momentum of the unstable spin mode.

Interestingly, when both scattering lengths are modulated simultaneously with the same frequency, the modulation amplitudes can be chosen such that parametric driving is present only in spin-independent or spin-dependent

interactions. Hence, it is possible to excite the density or spin mode alone during the initial stage of the dynamics. When the modulation frequencies differ, a fascinating scenario of competing instabilities appears. For instance, two momenta from either the density or spin mode become equally unstable, causing competition between the two wavelengths. In a classical fluid, two patterns with different symmetries coexist in the onset of competing instabilities [47]. In our case, the competing instabilities result in a superposition of Faraday patterns or a correlation function with different wavelengths whose amplitudes vary in time. To conclude, our studies reveal that the nature of driven dynamics in spinor condensates can be controlled by tuning the interaction strengths, quadratic Zeeman field, modulation frequencies, and amplitudes.

This paper is structured as follows. In Sec. II, we discuss the setup and the mean-field equations describing a spin-1 condensate. The Mathieu-like equations governing the wave-number selection of a driven spin-1 condensate are derived in Sec. III. The dynamics of driven ferromagnetic and polar phases, including the spin-spin correlations, are discussed in Secs. IV and V, respectively. Competing instabilities of different density or spin modes are discussed in Sec. VC 1. The experimental possibilities are discussed in Sec. VI. Finally, we summarize and provide an outlook in Sec. VII.

II. SETUP AND MODEL

We consider a Q2D spin-1 homogeneous Bose gas in the presence of a quadratic Zeeman field q . The Hamiltonian describing the system is

$$\hat{H} = \int d\rho \sum_{m=0,\pm 1} \hat{\psi}_m^\dagger(\rho) \left(-\frac{\hbar^2}{2M} \nabla_\rho^2 \right) \hat{\psi}_m(\rho) + \hat{H}_Z + \hat{V}_I, \quad (1)$$

where $\hat{\psi}_m$ is the field operator which annihilates a boson in the m th Zeeman state, M is the mass of a boson, and $\rho = (x, y)$. The quadratic Zeeman Hamiltonian is

$$\hat{H}_Z = q \int d\rho \sum_{m_1, m_2} \hat{\psi}_{m_1}^\dagger(\rho) (\hat{F}_z^2)_{m_1, m_2} \hat{\psi}_{m_2}(\rho), \quad (2)$$

and the interaction operator is

$$\hat{V}_I = \frac{1}{2} \int d\rho [\tilde{c}_0 : \hat{n}^2(\rho) : + \tilde{c}_1 : \hat{F}^2(\rho) :], \quad (3)$$

where $\tilde{c}_{0,1} = c_{0,1}/\sqrt{2\pi}l_z$, with $l_z = \sqrt{\hbar/m\omega_z}$ being the transverse width of the condensate provided by the harmonic potential $V_r(z) = m\omega_z^2 z^2/2$, and $\hat{n}(\rho) = \sum_{m=-f}^f \hat{\psi}_m^\dagger(\rho) \hat{\psi}_m(\rho)$ is the total density operator. The symbol $::$ denotes the normal ordering that places annihilation operators to the right of the creation operators. The components of the spin-density operator are

$$\hat{F}_{\nu \in x, y, z}(\rho) = \sum_{m, m'} (f_\nu)_{mm'} \hat{\psi}_m^\dagger(\rho) \hat{\psi}_{m'}(\rho), \quad (4)$$

with f_ν being the ν th component of the spin-1 matrices. The spin-independent and spin-dependent interaction constants are $c_0 = (g_0 + 2g_2)/3 > 0$ and $c_1 = (g_2 - g_0)/3$,

respectively, with $g_{\mathcal{F}} = 4\pi\hbar^2 a_{\mathcal{F}}/m$ related to the scattering length $a_{\mathcal{F}=0, 2}$ of the total spin- \mathcal{F} channel.

At very low temperatures the system is described by the coupled nonlinear Gross-Pitaevskii equations (NLGPEs), where $\hat{\psi}_m(\rho)$ is replaced by a c -number $\psi_m(\rho)$,

$$i\hbar \frac{\partial \psi_1}{\partial t} = \left[-\frac{\hbar^2 \nabla_\rho^2}{2M} + q + \tilde{c}_0 n + \tilde{c}_1 F_z \right] \psi_1 + \frac{\tilde{c}_1 F_-}{\sqrt{2}} \psi_0, \quad (5)$$

$$i\hbar \frac{\partial \psi_0}{\partial t} = \left[-\frac{\hbar^2 \nabla_\rho^2}{2M} + \tilde{c}_0 n \right] \psi_0 + \frac{\tilde{c}_1}{\sqrt{2}} F_+ \psi_1 + \frac{\tilde{c}_1 F_-}{\sqrt{2}} \psi_{-1}, \quad (6)$$

$$i\hbar \frac{\partial \psi_{-1}}{\partial t} = \left[-\frac{\hbar^2 \nabla_\rho^2}{2M} + q + \tilde{c}_0 n - \tilde{c}_1 F_z \right] \psi_{-1} + \frac{\tilde{c}_1 F_+}{\sqrt{2}} \psi_0, \quad (7)$$

where $F_\nu = \sum_{m, m'} \psi_m^*(f_\nu)_{mm'} \psi_{m'}$, $n(\rho, t) = \sum_m |\psi_m(\rho, t)|^2$, and $F_\pm = F_x \pm iF_y$. To study the modulation-induced dynamics, we solve Eqs. (5)–(7) numerically, starting from a homogeneous density embedded with a small noise in all three components [37,46].

III. TIME MODULATION OF s -WAVE SCATTERING LENGTHS

We consider a time-dependent $a_j(t) = \bar{a}_j [1 + 2\alpha_j \cos(2\omega_j t)]$, where \bar{a}_j is the mean scattering length, α_j is the modulation amplitude, and $2\omega_j$ is the driving frequency. Scattering lengths can be periodically modulated by Feshbach resonance [32,33,48] or using radio frequency or microwave fields [49–52]. We consider three cases: (i) a_0 is time dependent, and a_2 is constant, (ii) a_0 is constant, and a_2 is time dependent, and (iii) both a_0 and a_2 are time dependent. These cases can be implemented by independently controlling the two scattering lengths [53]. The interaction coefficients $\tilde{c}_{0,1}$ for the three cases are

$$\tilde{c}_0(t) = \bar{c}_0 + (2\alpha_0 \bar{g}_0/3) \cos(2\omega_0 t),$$

$$\tilde{c}_1(t) = \bar{c}_1 - (2\alpha_0 \bar{g}_0/3) \cos(2\omega_0 t)$$

for case (i),

$$\tilde{c}_0(t) = \bar{c}_0 + (4\alpha_2 \bar{g}_2/3) \cos(2\omega_2 t),$$

$$\tilde{c}_1(t) = \bar{c}_1 + (2\alpha_2 \bar{g}_2/3) \cos(2\omega_2 t)$$

for case (ii), and

$$\tilde{c}_0(t) = \bar{c}_0 + (2\alpha_0 \bar{g}_0/3) \cos(2\omega_0 t) + (4\alpha_2 \bar{g}_2/3) \cos(2\omega_2 t),$$

$$\tilde{c}_1(t) = \bar{c}_1 - (2\alpha_0 \bar{g}_0/3) \cos(2\omega_0 t) + (2\alpha_2 \bar{g}_2/3) \cos(2\omega_2 t)$$

for case (iii), where $\bar{c}_0 = (\bar{g}_0 + 2\bar{g}_2)/3$ and $\bar{c}_1 = (\bar{g}_2 - \bar{g}_0)/3$, with $\bar{g}_j = 4\pi\hbar^2 \bar{a}_j/(M\sqrt{2\pi}l_z)$.

The homogeneous solution in the presence of modulation is $\psi(t) = \sqrt{\bar{n}} \zeta \exp[-i\theta(t)/\hbar]$, where $\psi(t) = (\psi_1, \psi_0, \psi_{-1})^T$ and

$$\theta(t) = \int_0^t [\bar{n} \tilde{c}_0(t') + A \tilde{c}_1(t')] dt' + Bt, \quad (8)$$

where $A = [2n_0(n_1 + n_{-1}) + F_z^2 + 4n_0 \sqrt{n_1 n_{-1}}]/\bar{n}$ and $B = q(n_1 + n_{-1})/\bar{n}$, with $F_z = n_1 - n_{-1}$ and $n_m = \bar{n} \zeta_m^2$. Now,

we introduce

$$\psi(\rho, t) = [\sqrt{\bar{n}}\zeta + \mathbf{w}(t) \cos(\mathbf{k} \cdot \rho)]e^{-i\theta(t)/\hbar} \quad (9)$$

in Eqs. (5)–(7), where $\mathbf{w}(t) = (w_1, w_0, w_{-1})^T$ is the amplitude of the modulations, and we linearize in $\mathbf{w}(t)$. Writing $\mathbf{w}(t) = \mathbf{u}(t) + i\mathbf{v}(t)$, where $\mathbf{u} = (u_1, u_0, u_{-1})^T$ and $\mathbf{v} = (v_1, v_0, v_{-1})^T$ are real-valued vectors, we obtain the two first-order coupled differential equations:

$$-\hbar \frac{d\mathbf{v}}{dt} = (E_k \mathcal{I} + \mathcal{M}_1 + \mathcal{M}_2)\mathbf{u}, \quad (10)$$

$$\hbar \frac{d\mathbf{u}}{dt} = (E_k \mathcal{I} + \mathcal{M}_1 + \mathcal{M}_3)\mathbf{v}, \quad (11)$$

where $k = |\mathbf{k}|$, $E_k = \hbar^2 k^2 / 2M$, \mathcal{I} is a 3×3 identity matrix, and \mathcal{M}_1 is a time-independent diagonal matrix depending only on the Zeeman field with elements $(\mathcal{M}_1)_{11} = (\mathcal{M}_1)_{33} = q - B$ and $(\mathcal{M}_1)_{22} = -B$. However, $\mathcal{M}_{2,3}$ depend on the initial spinor ψ_m and are real, interaction- and time-dependent matrices. Equations (10) and (11) can be combined into a Mathieu-like second-order differential equation depending on the system parameters.

IV. FERROMAGNETIC PHASE

For an initial ferromagnetic phase with $\zeta = (1, 0, 0)^T$, the matrix \mathcal{M}_2 is diagonal in form with elements $(\mathcal{M}_2)_{11} = 2\bar{n}[\tilde{c}_0(t) + \tilde{c}_1(t)]$, $(\mathcal{M}_2)_{22} = 0$, and $(\mathcal{M}_2)_{33} = -2\bar{n}\tilde{c}_1(t)$, and \mathcal{M}_3 has only one nonzero element, $(\mathcal{M}_3)_{33} = -2\bar{n}\tilde{c}_1(t)$. The relevant Mathieu equation is

$$\frac{d^2 u_1}{dt^2} + \frac{1}{\hbar^2} [\epsilon_{k,1}^2 + 4\bar{n}E_k \alpha_2 \bar{g}_2 \cos(2\omega_2 t)] u_1 = 0, \quad (12)$$

where

$$\epsilon_{k,1} = \sqrt{E_k [E_k + 2(\bar{c}_0 + \bar{c}_1)\bar{n}]} \quad (13)$$

is the Bogoliubov dispersion describing the density excitations [35]. The dynamical stability of the uniform ferromagnetic phase demands $\bar{c}_0 + \bar{c}_1 > 0$ (real $\epsilon_{k,1}$). Since Eq. (12) is independent of α_0 , the ferromagnetic state is immune to the parametric driving of a_0 . The reason is that periodic modulation of a_0 causes equal and out-of-phase oscillations in \tilde{c}_0 and \tilde{c}_1 , which cancel each other.

According to the Floquet theorem, the solutions of Eq. (12) are $u_1(t) = b(t) \exp(\sigma t)$, where $b(t) = b(t + \pi/\omega_2)$ and $\sigma(k, \omega_2, \alpha)$ is called the Floquet exponent. If $\text{Re}(\sigma) > 0$, the ferromagnetic state is dynamically unstable against the formation of transient density modulations or Faraday patterns [see insets in Fig. 1(a)]. The pattern size is determined by the most unstable momentum k_u , i.e., momentum for which σ is the largest. For vanishing modulation amplitude ($\alpha_2 \rightarrow 0$), k_u is determined by the resonance $\epsilon_{k,1} = \hbar\omega_2$, and the corresponding Floquet exponent is $\sigma \simeq \bar{n}E_{k_u} \alpha_2 \bar{g}_2 / \hbar^2 \omega_2$ [3]. Since $\epsilon_{k,1}$ is a monotonously increasing function of k , k_u increases with ω_2 [see the unstable momentum rings in Figs. 1(b) and 1(c) for two different frequencies]. This implies that the pattern size decreases monotonously with increasing driving frequency ω_2 . At longer times, the higher harmonics ($\epsilon_{k,1} = j\hbar\omega_2$, with $j = 2, 3, \dots$) become relevant, causing the emergence of other rings of higher $|\mathbf{k}|$ in the momentum density, thus heating and destroying the condensate [54,55].

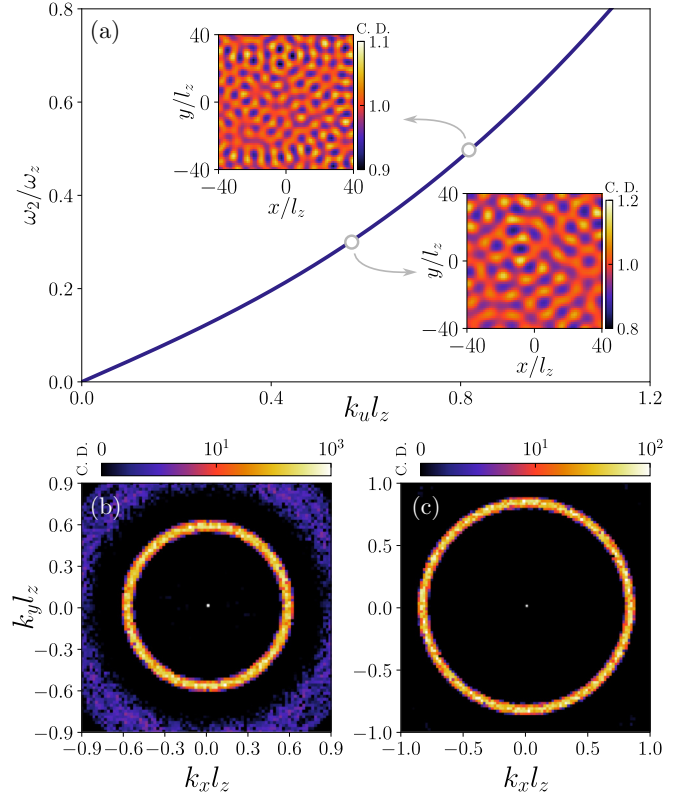


FIG. 1. Wave-number selection of an initial ferromagnetic homogeneous phase for a_2 modulation, $\bar{c}_0 \bar{n} = 0.3\hbar\omega_z$, $\bar{c}_1 \bar{n} = -0.1\hbar\omega_z$, $q = -0.3\hbar\omega_z$, and $\alpha_2 = 0.4$. (a) The most unstable momentum k_u as a function of driving frequency ω_2 . The insets show the numerical results of Faraday patterns. (b) and (c) The corresponding condensate momentum density for $\omega_2 t = 330$ and $\omega_2 t = 250$, respectively. C.D. stands for condensate density, and in (b) and (c), the central peak at $k = 0$ is removed to improve the visibility of the momentum rings.

V. POLAR PHASE

For the polar phase $\zeta_p = (0, 1, 0)^T$, the chemical potential is $\mu_{2D} = \bar{c}_0 \bar{n}$, and we have

$$\mathcal{M}_2 = \bar{n} \begin{bmatrix} \tilde{c}_1(t) & 0 & \tilde{c}_1(t) \\ 0 & 2\tilde{c}_0(t) & 0 \\ \tilde{c}_1(t) & 0 & \tilde{c}_1(t) \end{bmatrix},$$

$$\mathcal{M}_3 = \bar{n}\tilde{c}_1(t) \begin{bmatrix} 1 & 0 & -1 \\ 0 & 0 & 0 \\ -1 & 0 & 1 \end{bmatrix}.$$

We get the Mathieu-like equations

$$\frac{d^2 u_0}{dt^2} + \frac{1}{\hbar^2} E_k [E_k + 2\bar{n}\tilde{c}_0(t)] u_0 = 0, \quad (14)$$

$$\frac{d^2 u_+}{dt^2} + \frac{1}{\hbar^2} (E_k + q) [E_k + q + 2\bar{n}\tilde{c}_1(t)] u_+ = 0, \quad (15)$$

where $u_+ = u_1 + u_{-1}$. Unlike the ferromagnetic case, both the density and spin modes,

$$\epsilon_{k,0} = \sqrt{E_k (E_k + 2\bar{c}_0 \bar{n})}, \quad (16)$$

$$\epsilon_{k,\pm 1} = \sqrt{(E_k + q)(E_k + q + 2\bar{c}_1 \bar{n})}, \quad (17)$$

become important for the dynamics. $\epsilon_{k,0}$ corresponds to the density modulations (phonons) and the degenerate $\epsilon_{k,\pm 1}$ modes associated with the elementary process of $(\mathbf{0}, 0) + (\mathbf{0}, 0) \leftrightarrow (\mathbf{k}, \pm 1) + (-\mathbf{k}, \mp 1)$. When $q = 0$ and $\bar{c}_0 = \bar{c}_1$, all three modes are degenerate. The dynamical stability of the homogeneous polar phase demands $\bar{c}_0 > 0$, $q(q + 2\bar{c}_1\bar{n}) \geq 0$, and $q + \bar{c}_1\bar{n} \geq 0$. Below we consider the three cases of modulation. In the numerical calculations in Eqs. (5)–(7), the initial polar phase is embedded with a noise field $\delta(\rho)$ populating the vacuum modes in the limit $q \rightarrow \infty$ based on the truncated Wigner prescription [46,56],

$$\delta(\rho) = \frac{1}{\sqrt{V}} \sum_{\mathbf{k}} \begin{pmatrix} \alpha_{\mathbf{k}}^{+1} \exp(i\mathbf{k} \cdot \rho) \\ \alpha_{\mathbf{k}}^0 u_{\mathbf{k}} \exp(i\mathbf{k} \cdot \rho) + \alpha_{\mathbf{k}}^{0*} v_{\mathbf{k}} \exp(-i\mathbf{k} \cdot \rho) \\ \alpha_{\mathbf{k}}^{-1} \exp(i\mathbf{k} \cdot \rho) \end{pmatrix}, \quad (18)$$

where V is the volume, $\alpha_{\mathbf{k}}^m$ are complex Gaussian random variables with zero mean and satisfy $\langle \alpha_{\mathbf{k}}^{m*} \alpha_{\mathbf{k}'}^{m'} \rangle = (1/2) \delta_{mm'} \delta_{\mathbf{k}\mathbf{k}'}$, and the amplitudes are given by

$$u_{\mathbf{k}} = \sqrt{\frac{E_k + c_0\bar{n}}{2\sqrt{E_k(E_k + 2c_0\bar{n})}}} - \frac{1}{2}, \quad (19)$$

$$v_{\mathbf{k}} = \sqrt{1 - u_{\mathbf{k}}^2}. \quad (20)$$

We also found qualitatively similar results for the initial state

$$\psi(\rho, t = 0) = \begin{pmatrix} p_{+1} \exp(i\theta_1) \\ [1 - p_{+1}^2 - p_{-1}^2] \exp(i\theta_0) \\ p_{-1} \exp(i\theta_{-1}) \end{pmatrix}, \quad (21)$$

with a noise from a uniform distribution, where p_{α} and θ_{α} are random numbers with $p_{\pm 1} \ll 1$.

A. a_0 modulation

For a_0 modulation, the Mathieu equations (14) and (15) become

$$\frac{d^2 u_0}{dt^2} + \frac{1}{\hbar^2} \left[\epsilon_{k,0}^2 + \frac{4\bar{n}E_k\alpha_0\bar{g}_0}{3} \cos(2\omega_0 t) \right] u_0 = 0, \quad (22)$$

$$\frac{d^2 u_{\pm}}{dt^2} + \frac{1}{\hbar^2} \left[\epsilon_{k,\pm 1}^2 - \frac{4\bar{n}(E_k + q)\alpha_0\bar{g}_0}{3} \cos(2\omega_0 t) \right] u_{\pm} = 0. \quad (23)$$

For a given ω_0 in the limit $\alpha_0 \rightarrow 0$, the resonances $\epsilon_{k,0} = \hbar\omega_0$ and $\epsilon_{k,\pm 1} = \hbar\omega_0$ provide two unstable momenta $k_u^{(0)}$ and $k_u^{(\pm)}$ with Floquet exponents $\sigma^{(0)} \simeq \bar{n}E_{k_u^{(0)}}\alpha_0\bar{g}_0/3\hbar^2\omega_0$ and $\sigma^{(\pm)} \simeq \bar{n}(E_{k_u^{(\pm)}} + q)\alpha_0\bar{g}_0/3\hbar^2\omega_0$. Using $k_u^{(0)}$ and $k_u^{(\pm)}$ obtained from the resonance conditions, we rewrite the Floquet exponents as

$$\sigma^{(0)} = \frac{\alpha_0\bar{n}\bar{g}_0}{3\hbar^2\omega_0} \left[\sqrt{(\bar{n}\bar{c}_0)^2 + \hbar^2\omega_0^2} - \bar{n}\bar{c}_0 \right], \quad (24)$$

$$\sigma^{(\pm)} = \frac{\alpha_0\bar{n}\bar{g}_0}{3\hbar^2\omega_0} \left[\sqrt{(\bar{n}\bar{c}_1)^2 + \hbar^2\omega_0^2} - \bar{n}\bar{c}_1 \right]. \quad (25)$$

When $\bar{c}_0 = \bar{c}_1$, $\sigma^{(0)} = \sigma^{(\pm)}$, and interestingly, $\sigma^{(\pm)}$ is independent of the quadratic Zeeman field q , which has interesting consequences, as we discuss later.

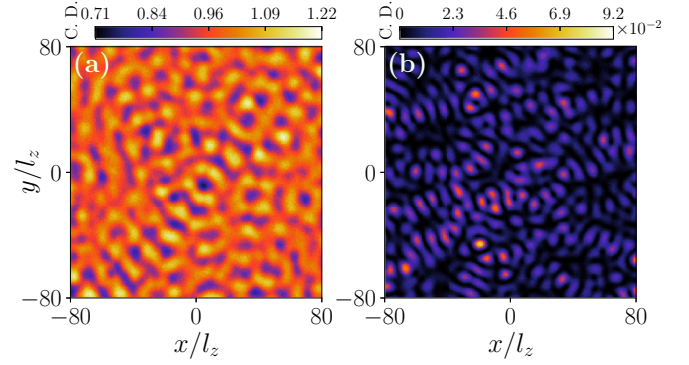


FIG. 2. Density patterns for a_0 modulation on an initial polar phase. The parameters are $q = 0$, $\bar{c}_0\bar{n} = \bar{c}_1\bar{n} = 0.2\hbar\omega_z$, $\alpha_0 = 0.4$, and $\omega_0/\omega_z = 0.2$ at $\omega_z t = 600$. The density pattern in (b) $m = \pm 1$ differs from that of (a) $m = 0$. C.D. stands for condensate density.

1. Degenerate modes

When all three modes are degenerate (when $q = 0$ and $\bar{c}_1 = \bar{c}_0$), $k_u^{(0)} = k_u^{(\pm)} = k_u$, and $\sigma^{(0)} = \sigma^{(\pm)}$, which implies that both density and spin modes get populated simultaneously by periodic driving. The unstable density mode $\epsilon_{k,0}$ leads to the formation of Faraday patterns [see Fig. 2(a)] or, equivalently, the exponential growth of atoms with finite momenta in the $m = 0$ component, shown as $N_{0,k \neq 0}$ in Fig. 3. The unstable $\epsilon_{k,\pm 1}$ modes initiate the population transfer from $m = 0$ to $m = \pm 1$, leading to the spin dynamics seen in Fig. 3. At the initial stage, the population in $m = \pm 1$ grows exponentially at a rate determined by $\sigma^{(\pm)}$ and exhibits oscillations of frequency $2\omega_0$. Eventually, a density pattern also develops in the $m = \pm 1$ components [see Fig. 2(b)].

The momentum density of $m = 0$ is shown in Fig. 4 at two different instances. In the early stages of the pattern formation, the most unstable momenta are given by the resonance

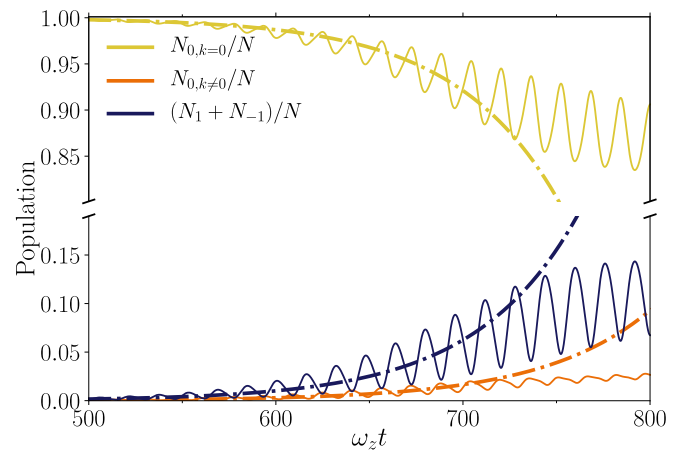


FIG. 3. Population dynamics for a_0 modulation and $q = 0$. Other parameters are $\bar{c}_0\bar{n} = \bar{c}_1\bar{n} = 0.2\hbar\omega_z$, $\alpha_0 = 0.4$, and $\omega_0/\omega_z = 0.2$. The population in each component is $N_m(t) = \int |\psi_m(x, y, t)|^2 dx dy$, the total population $N = \sum_m N_m$, the population with $k \neq 0$ in $m = 0$ is $N_{0,k \neq 0} = \int_{k \neq 0} dk_x dk_y |\tilde{\psi}_0(k_x, k_y, t)|^2$, and the zero-momentum population in $m = 0$ is $N_{0,k=0}$. The dash-dotted lines show the exponential fit determined by the Floquet exponent, and the solid lines are from the numerical calculations of NLGPEs.

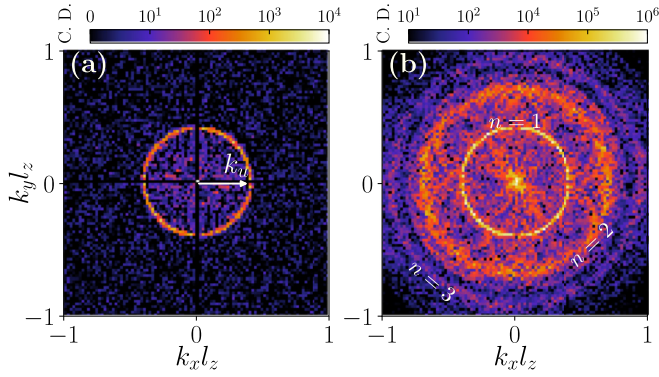


FIG. 4. The momentum density of the $m = 0$ component at (a) $\omega_z t = 300$ and (b) $\omega_z t = 650$ for $\bar{c}_0 \bar{n} = \bar{c}_1 \bar{n} = 0.2 \hbar \omega_z$, $\alpha_0 = 0.4$, and $\omega_0/\omega_z = 0.2$. The momentum ring in (a) and the primary one in (b) are given by the resonance $\epsilon_{k,0} = \hbar \omega_0$. Two higher harmonics can also be seen in (b). C.D. stands for the condensate density, and the central peak at $k = 0$ is removed to improve the visibility of the momentum rings.

condition $\epsilon_{k,0} = \hbar \omega_0$, which we mark by k_u in Fig. 4(a). Although the next leading unstable momenta come from the second harmonics $\epsilon_{k,0} = 2\hbar \omega_0$, there are also contributions from processes in which a pair of atoms, each from $m = +1$ and $m = -1$ with momenta of magnitudes $(k_u, -k_u)$ or $(\pm k_u, \pm k_u)$, scatters into $(+\mathbf{k}, -\mathbf{k})$ or $(\mathbf{k}, \mathbf{k}')$ with $|\mathbf{k} + \mathbf{k}'| = 2k_u$. All such \mathbf{k} and \mathbf{k}' lead to a disk-shaped pattern in the momentum space of the condensate wave function in addition to the harmonics, but with lower amplitudes, as shown in Fig. 4(b). At longer times, the condensate gets destroyed by heating.

Magnetization dynamics. The initial polar condensate has a null spin-density vector \mathbf{F} . The spin-mixing dynamics in Fig. 3 leads to the emergence of the spin textures shown in Fig. 5(a). Strikingly, the velocity field of the transverse spin-density vector $\mathbf{F}_\perp(x, y)$ in Fig. 5(b) reveals the formation of PCVs and antivortices [34,57,58]. They are marked by circles in Figs. 5(a) and 5(b). The core of a PCV is filled with $m = 0$ atoms with no vorticity, and the surrounding $m = +1$ and $m = -1$ atoms have opposite vorticities. Figure 5(c) shows the time dependence of vortex density N_v/L^2 , where L^2 is the area of the numerical box we use. The vortex number N_v is determined by computing the phase winding at the smallest loops defined by the grid size. At $t = 0$, the initial random noise in the $m = \pm 1$ components contributes to the vortex number N_v , which eventually decays over time as the PCVs materialize. N_v decreases until the number of PCVs reaches a steady value $N_v^{(\text{PCV})}$ and the decay rate is determined by $\sigma^{(+)}$.

Since the amplitude of the spin texture oscillates in time with the driving frequency, N_v exhibits the same oscillations. When the spin-texture amplitude is tiny, N_v becomes large from the noise contribution. If the amplitude is sufficiently large, the noise is overshadowed. Once N_v reaches a steady value, the minima shown in the inset of Fig. 5(c) approximately provide us with the number of PCVs. Interestingly, $N_v^{(\text{PCV})}$ is determined by the unstable momentum k_u , as shown in Fig. 5(c), and as expected, it exhibits k_u^2 behavior. This implies that the larger the modulation frequency is, the denser the spin-vortex gas is. At longer times ($\sigma^{(+)}t > 16$), we observed

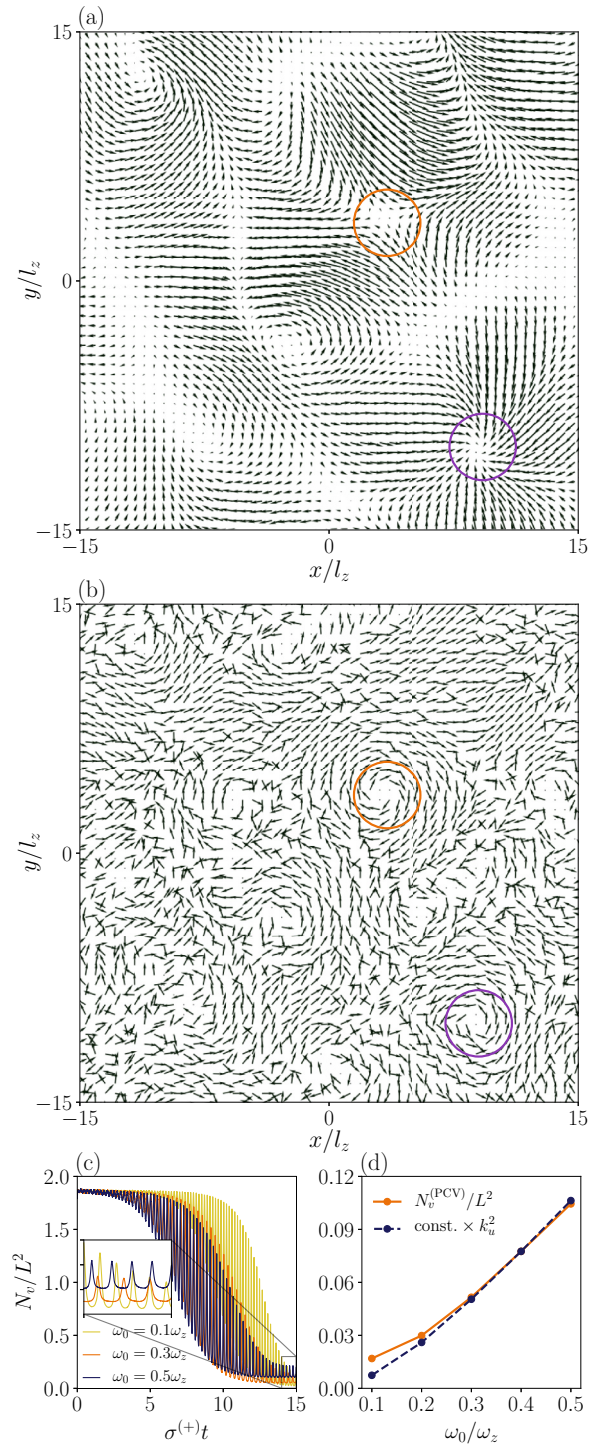


FIG. 5. Spin textures for a_0 modulation and $q = 0$. (a) The transverse spin density $\mathbf{F}_\perp(x, y)$ and (b) the velocity field of $\mathbf{F}_\perp(x, y) = (F_x, F_y)$, i.e., $\vec{\nabla}\phi/|\vec{\nabla}\phi|$, where $\phi = \arctan(F_x/F_y)$ at $\omega_z t = 670$ or $\sigma^{(+)}t = 14.74$. Other parameters are the same as in Fig. 3. Both vortices and antivortices are marked in (b). (c) The dynamics of the vortex density N_v/L^2 , where L is the numerical box size, is obtained by averaging over 10 realizations of noises. It decreases in time and eventually saturates. (d) The saturated vortex density (before the condensate is destroyed, taken around $\sigma^{(+)}t = 15$) as a function of driving frequency ω_0 , which exhibits a quadratic dependence on the most unstable momentum. The latter is expected, considering the Q2D nature of the condensate.

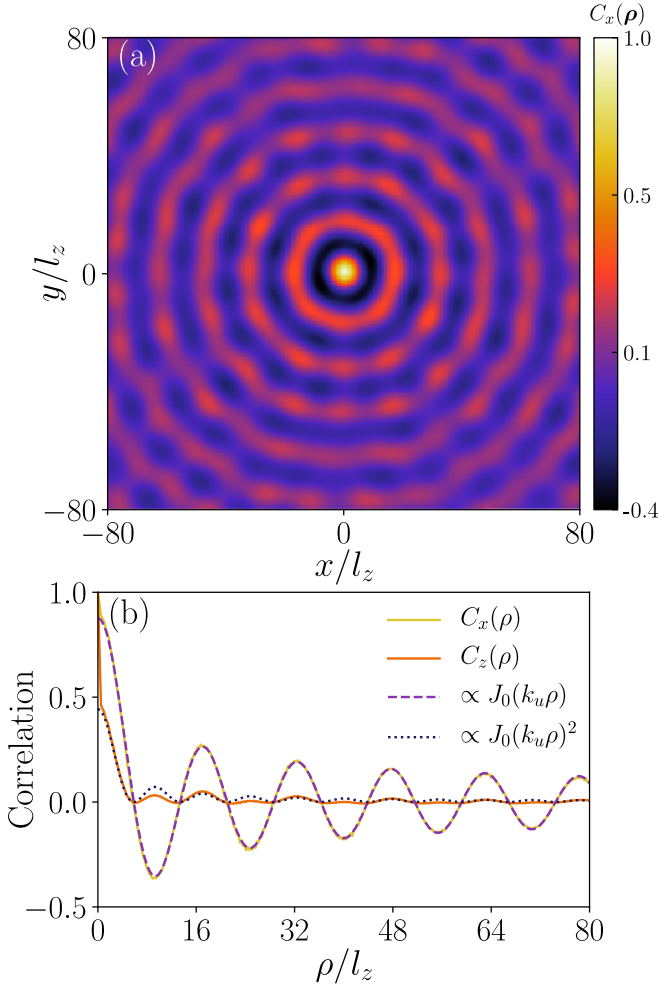


FIG. 6. Spin-spin correlations for a_0 modulation and $q = 0$. (a) The transverse magnetization correlation $C_x(\rho, t)$ in the xy plane and (b) the radial correlation function $C_{x,z}(\rho)$ at $\omega_z t = 500$. Other parameters are the same as in Fig. 3. We see that $C_{x,y}(\rho) \propto J_0(k_u \rho)$ and $C_z(\rho) \propto J_0^2(k_u \rho)$. The plots are obtained by taking an average of results from 10 different realizations of initial noise.

that the $m = 0$ homogeneous condensate gets significantly depleted, and PCVs disintegrate into independent gases of vortices in the $m = 1$ and $m = -1$ components.

Further, we analyze the scaled spin-spin correlations,

$$C_\alpha(\rho, t) = \frac{1}{N_\alpha} \iint d\rho' F_\alpha(\rho + \rho', t) F_\alpha(\rho', t), \quad (26)$$

where $\alpha \in \{x, y, z\}$ and $N_\alpha = \iint d\rho F_\alpha(\rho)^2$. $C_x(\rho, t)$ at an instant well before the condensate is destroyed is shown in Fig. 6(a). The radial correlations along the transverse and longitudinal magnetization densities $C_\alpha(\rho) = (1/2\pi) \int_0^{2\pi} C_\alpha(\rho) d\theta$ are found to be governed by the Bessel function $J_0(k_u \rho)$, where $\rho = |\rho|$ and, in particular, $C_{x,y}(\rho) \propto J_0(k_u \rho)$ and $C_z(\rho) \propto J_0^2(k_u \rho)$ [see Fig. 6(b)]. Similar Bessel correlations are predicted in spinor condensates subjected to quantum quenches [45,56,59].

2. Nondegenerate modes

For $q \neq 0$ or $\bar{c}_1 \neq \bar{c}_0$, the degeneracy between the density ($\epsilon_{k,0}$) and spin ($\epsilon_{k,\pm 1}$) modes is lifted, and consequently,

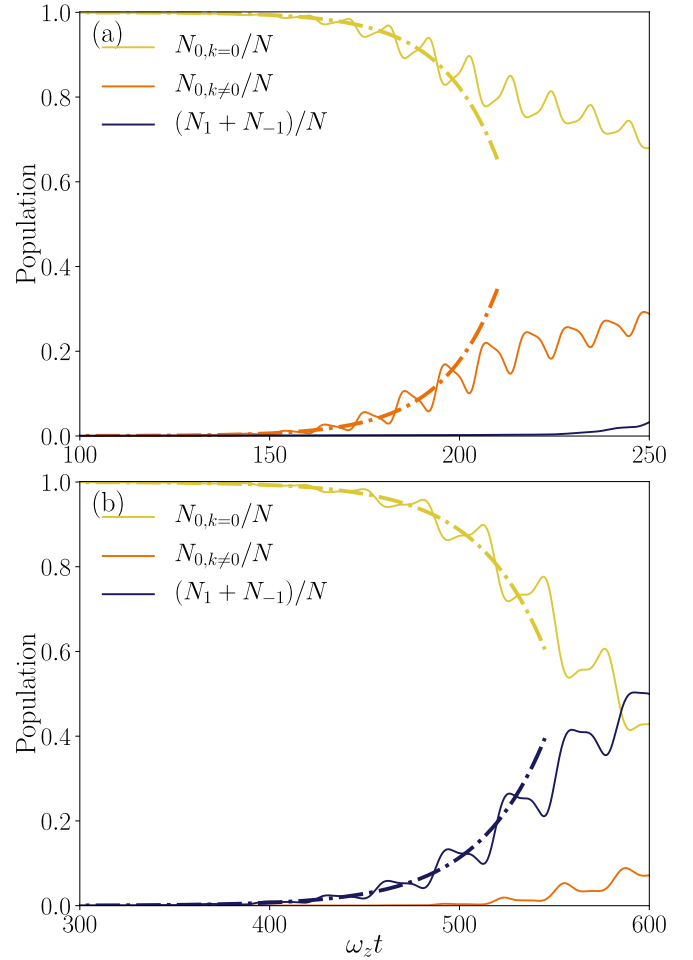


FIG. 7. The population dynamics for a_0 modulation and $q = 0$. (a) $\bar{c}_0 \bar{n} = 0.2 \hbar \omega_z$, $\bar{c}_1 \bar{n} = 4 \hbar \omega_z$, $\alpha_0 = 0.03$, and $\omega_0/\omega_z = 0.3$. (b) $\bar{c}_0 \bar{n} = 0.4 \hbar \omega_z$, $\bar{c}_1 \bar{n} = 0.05 \hbar \omega_z$, $\alpha_0 = 0.25$, and $\omega_0/\omega_z = 0.1$. In (a) $N_{0,k \neq 0}$ outgrows $N_{\pm 1}$, with the reverse in (b). The solid lines are the numerical results, and dot-dashed lines are the exponential fit provided by $\sigma^{(0)}$.

$k_u^{(0)} \neq k_u^{(+)}$. First, we consider $q = 0$ and $\bar{c}_1 \neq \bar{c}_0$. If $\sigma^{(0)}$ and $\sigma^{(+)}$ are comparable, the dynamics remains qualitatively the same as in the case of degenerate modes. So we consider the two extreme scenarios: $\bar{c}_0 \ll \bar{c}_1$ and $\bar{c}_1 \ll \bar{c}_0$. For $\bar{c}_0 \ll \bar{c}_1$, the density mode is the soft one, and consequently, $\sigma^{(0)} \gg \sigma^{(+)}$. In that case, the Faraday pattern in $m = 0$ forms well before the spin-mixing dynamics takes place [see the dynamics of $N_{0,k \neq 0}$ and $N_{\pm 1}$ in Fig. 7(a)]. The initial growth of $N_{0,k \neq 0}$ is determined by $\sigma^{(0)}$ [dot-dashed line in Fig. 7(a)]. By the time the population transfer to $m = \pm 1$ takes place, the homogeneous condensate in $m = 0$ is significantly altered and depleted, making our linear stability analysis invalid. In contrast, for $\bar{c}_0 \gg \bar{c}_1$, $N_{\pm 1}$ outgrows $N_{0,k \neq 0}$ [see Fig. 7(b)], and the initial dynamics is governed by $\sigma^{(+)}$. The spin dynamics leads to spin textures and the formation of PCVs. The spin-spin correlations have different behaviors for the two extreme cases. For $\bar{c}_0 \ll \bar{c}_1$, $C_{x,y,z}(\rho)$ decays exponentially (see Fig. 8) with a correlation length of the order of a spin healing length, which is proportional to $1/\sqrt{\bar{c}_1 \bar{n}}$, whereas for $\bar{c}_1 \ll \bar{c}_0$, they exhibit

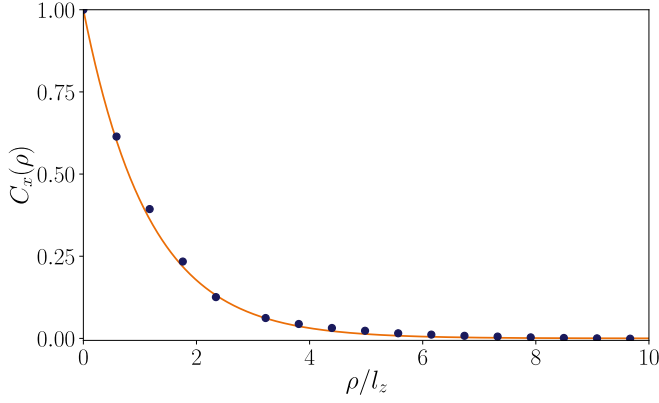


FIG. 8. The radial transverse spin-spin correlation function $C_x(\rho)$ for $\bar{c}_0\bar{n} = 0.2\hbar\omega_z$, $\bar{c}_1\bar{n} = 4\hbar\omega_z$, $\alpha_0 = 0.03$, and $\omega_0/\omega_z = 0.3$, exhibiting exponential decay at the instant $\omega_z t = 240$. The dots are obtained from the average of results from 10 different realizations of initial noise. The solid line is an exponential fit. The corresponding population dynamics is shown in Fig. 7(a).

a Bessel function dependence of $C_{x,y}(\rho) = J_0(k_u^{(+)}\rho)$ and $C_z(\rho) = J_0^2(k_u^{(+)}\rho)$.

Nonzero q . The nature of the dynamics also depends critically on the quadratic Zeeman field q . A finite q not only lifts the degeneracy of the modes but also introduces a gap, $\Delta = \sqrt{q(q + 2\bar{c}_1\bar{n})}$, in the spin modes [see Fig. 9(a)]. This means that there is no spin-mixing dynamics if the driving frequency lies below the gap ($\omega_0 < \Delta$), and the periodic modulation leads to forming only the Faraday pattern in $m = 0$. In contrast, for $\omega_0 \geq \Delta$, both spin and density modes contribute to the dynamics. Since the Mathieu exponents are independent of q [see Eqs. (24) and (25)], both modes are unstable simultaneously for $\bar{c}_1 = \bar{c}_0$. In that case, the dynamics is identical to the case for degenerate modes, but the momenta governing the Faraday pattern and the vortex density are different, i.e., $k_u^{(0)} \neq k_u^{(+)}$. The spatial dependence of spin-spin correlations is governed by $k_u^{(+)}$ via the Bessel function.

Even though the Mathieu exponents are independent of q , the above results indicate an implicit dependence of q on the

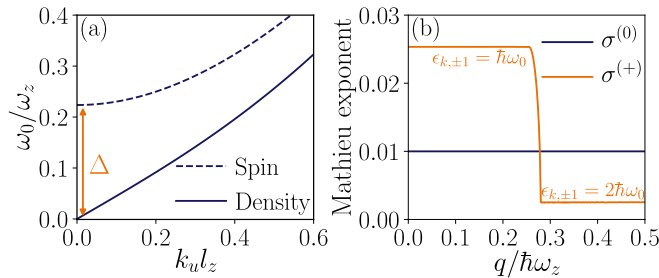


FIG. 9. (a) The Bogoliubov spectrum for $\bar{c}_0\bar{n} = \bar{c}_1\bar{n} = 0.2\hbar\omega_z$, $\omega_0/\omega_z = 0.3$, and $q = 0.1\hbar\omega_z$. The unstable momenta as a function of ω_0 map the spectrum in the limit $\alpha \rightarrow 0$. (b) The Mathieu exponents of density and spin modes as a function of q for $\bar{c}_0\bar{n} = 0.4\hbar\omega_z$, $\bar{c}_1\bar{n} = 0.05\hbar\omega_z$, $\omega_0/\omega_z = 0.3$, and $\alpha_0 = 0.3$. Δ is the gap of the spin modes at $k = 0$. In (b), the primary resonance associated with the spin mode changes from $\epsilon_{k,\pm 1} = \hbar\omega_0$ to $\epsilon_{k,\pm 1} = 2\hbar\omega_0$ as a function of q , leading to a significant decrease in the Mathieu exponent $\sigma^{(+)}$.

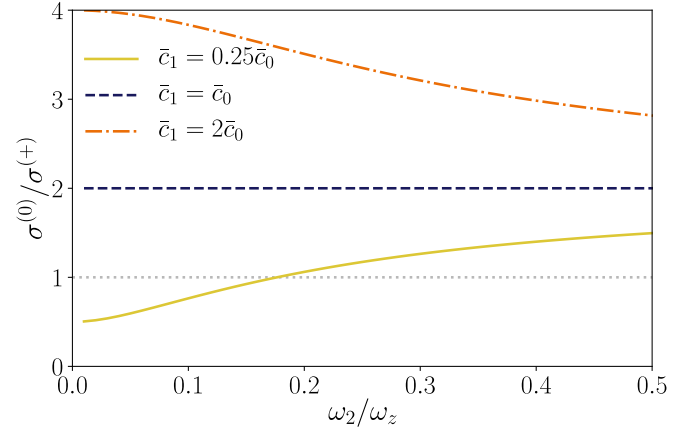


FIG. 10. The results for a_2 modulation. $\sigma^{(0)}/\sigma^{(+)}$ as a function of ω_2 for $\bar{c}_0\bar{n} = 0.2\hbar\omega_z$ and $q = 0$ with different \bar{c}_1/\bar{c}_0 . For $\bar{c}_0 = \bar{c}_1$, we get $\sigma^{(0)}/\sigma^{(+)} = 2$ (dashed line), and for $\bar{c}_1 < \bar{c}_0$ (solid line), the value of $\sigma^{(0)}/\sigma^{(+)}$ crosses 1, which indicates there is a change in the behavior of dynamics above and below a critical driving frequency ($\omega_2 \approx 0.18\omega_z$).

dynamics for a fixed ω_0 . For instance, for sufficiently small q such that $\Delta < \omega_0$, both modes are unstable simultaneously, whereas for sufficiently large q such that $\Delta > \omega_0$, only the density mode is unstable. A similar scenario, as shown in Fig. 9(b), also emerges for $\bar{c}_1 \ll \bar{c}_0$. For small q , the spin dynamics dominates ($\sigma^{(+)} \gg \sigma^{(0)}$), and for large q , only the Faraday pattern is formed. When the spin-mixing dynamics dominates ($\bar{c}_1 \ll \bar{c}_0$), the spin-spin correlations are again governed by the Bessel functions as before.

B. a_2 modulation

For a_2 modulation, the Mathieu equations (14) and (15) become

$$\frac{d^2 u_0}{dt^2} + \frac{1}{\hbar^2} \left[\epsilon_{k,0}^2 + \frac{8\bar{n}E_k\alpha_2\bar{g}_2}{3} \cos(2\omega_2 t) \right] u_0 = 0, \quad (27)$$

$$\frac{d^2 u_{\pm}}{dt^2} + \frac{1}{\hbar^2} \left[\epsilon_{k,\pm 1}^2 + \frac{4\bar{n}(E_k + q)\alpha_2\bar{g}_2}{3} \cos(2\omega_2 t) \right] u_{\pm} = 0. \quad (28)$$

The Mathieu exponents for the density and spin modes are obtained as

$$\sigma^{(0)} = \frac{2\alpha_2\bar{n}\bar{g}_2}{3\hbar^2\omega_2} \left[\sqrt{(\bar{n}\bar{c}_0)^2 + \hbar^2\omega_2^2} - \bar{n}\bar{c}_0 \right], \quad (29)$$

$$\sigma^{(+)} = \frac{\alpha_2\bar{n}\bar{g}_2}{3\hbar^2\omega_2} \left[\sqrt{(\bar{n}\bar{c}_1)^2 + \hbar^2\omega_2^2} - \bar{n}\bar{c}_1 \right]. \quad (30)$$

In comparison to the case with a_0 modulation [Eq. (24)], an additional factor of 2 appears in Eq. (29). Therefore, we expect different dynamics for a_2 modulation for a given set of interaction parameters. The results of a_2 modulation for $q = 0$ are summarized in Fig. 10, where we show the ratio of Mathieu exponents associated with the density and spin modes as a function of the driving frequency. For degenerate modes, i.e., when $\bar{c}_1 = \bar{c}_0$ (dashed line in Fig. 9), $\sigma^{(0)} = 2\sigma^{(+)}$, which

means the Faraday pattern emerges well before the spin-mixing occurs. That is also the case for $\bar{c}_1 > \bar{c}_0$ (dot-dashed line in Fig. 9). Interestingly, for $\bar{c}_1 < \bar{c}_0/2$, the nature of the dynamics depends on ω_2 . For smaller ω_2 , $\sigma^{(0)}/\sigma^{(+)} < 1$; that is, spin mixing dominates the density modulations, and the opposite occurs for large values of ω_2 . Making q nonzero would lead to an explicit dependence of ω_2 on the dynamics for any value of \bar{c}_0 and \bar{c}_1 , but qualitative features remain the same.

C. Modulation of both a_0 and a_2

As we have seen in the previous cases, an implicit competition exists between the density modulations (Faraday patterns) and spin mixing. By controlling interaction strengths, quadratic Zeeman field, or the driving frequencies, we can access different scenarios in which one dominates or both co-occur in the dynamics. Further, we show greater controllability is achieved by simultaneously modulating a_0 and a_2 . To do so, we assume a phase difference ϕ between a_0 and a_2 modulations, i.e., $a_2(t) = \bar{a}_2[1 + 2\alpha_2 \cos(2\omega_2 t + \phi)]$. Strikingly, taking $\omega_0 = \omega_2$, $\alpha_2 = \alpha_0 \bar{g}_0/\bar{g}_2$, and $\phi = 0$ is equivalent to modulating \bar{c}_0 while keeping \bar{c}_1 constant. In that case, Eqs. (14) and (15) become

$$\frac{d^2 u_0}{dt^2} + \frac{1}{\hbar^2} [\epsilon_{k,0}^2 + 4\bar{n}E_k \alpha_0 \bar{g}_0 \cos(2\omega_0 t)] u_0 = 0, \quad (31)$$

$$\frac{d^2 u_{\pm}}{dt^2} + \frac{1}{\hbar^2} \epsilon_{k,\pm 1}^2 u_{\pm} = 0. \quad (32)$$

The above equations convey that Faraday patterns are formed in $m = 0$, but spin mixing does not occur. The numerical calculations of NLGPEs also confirm this. If we take $\phi = \pi$ and $\alpha_2 = \alpha_0 \bar{g}_0/2\bar{g}_2$, \bar{c}_1 becomes periodic in time, and \bar{c}_0 remains a constant. The corresponding equations of motion are

$$\frac{d^2 u_0}{dt^2} + \frac{1}{\hbar^2} \epsilon_{k,0}^2 u_0 = 0, \quad (33)$$

$$\frac{d^2 u_{\pm}}{dt^2} + \frac{1}{\hbar^2} [\epsilon_{k,\pm 1}^2 + 2\bar{n}(E_k + q)\alpha_0 \bar{g}_0 \cos(2\omega_0 t)] u_{\pm} = 0. \quad (34)$$

In this case, the spin mode is unstable, leading to the population transfer from $m = 0$ to $m = \pm 1$. The latter causes local depletions in the homogeneous density of $m = 0$ and random density peaks that emerge in $m = \pm 1$ components [see Figs. 11(a) and 11(b)]. The momentum ring in the momentum density of $m = \pm 1$ [see Fig. 11(d)] arises from the spin-mixing process, $(\mathbf{0}, 0) + (\mathbf{0}, 0) \leftrightarrow (\mathbf{k}, \pm 1) + (-\mathbf{k}, \mp 1)$. In contrast, the process in which a pair of atoms, each in $m = +1$ and $m = -1$ with momenta $(k_u, -k_u)$ or $(\pm k_u, \pm k_u)$, scatters into $(+\mathbf{k}, -\mathbf{k})$ or $(\mathbf{k}, \mathbf{k}')$ with $|\mathbf{k} + \mathbf{k}'| = 2k_u$ populates the nonzero momenta in $m = 0$ [see Fig. 11(c)] at a later time. It is starkly different from Fig. 4(b) with the pure a_0 modulation where the primary unstable momenta come from the resonance with the density mode.

1. Competing instabilities

We show that by modulating a_0 and a_2 with $\omega_0 \neq \omega_2$ and carefully choosing the modulation amplitudes α_0 and α_2 ,

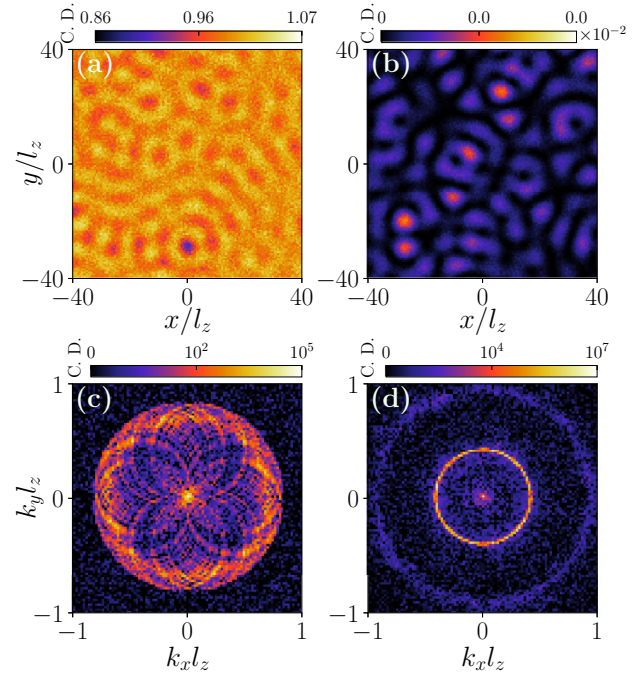


FIG. 11. Results for simultaneous modulation of a_0 and a_2 with a phase difference of $\phi = \pi$. Real-space condensate density of (a) $m = 0$ and (b) $m = \pm 1$ for $q = 0$, $\bar{c}_0 \bar{n} = \bar{c}_1 \bar{n} = 0.2\hbar\omega_z$, $\alpha_0 = 0.2$, $\alpha_2 = 0.05$, and $\omega_0/\omega_z = \omega_2/\omega_z = 0.2$ at $\omega_z t = 800$. The corresponding momentum densities are shown in (c) and (d).

the intriguing scenario of competing instabilities emerges. In particular, two distinct momenta of the density or spin mode compete. To see the competing instabilities among the density modes, we take $\bar{c}_0 \ll \bar{c}_1$ such that $\sigma^{(0)} \gg \sigma^{(+)}$. The primary resonances that emerge from modulating a_0 and a_2 are $\epsilon_{k,0} = \hbar\omega_0$ and $\epsilon_{k,0} = \hbar\omega_2$ and let the corresponding unstable momenta and Mathieu exponents be $(k_{u0}^{(0)}, k_{u2}^{(0)})$ and $(\sigma_0^{(0)}, \sigma_2^{(0)})$. The relevant equation of motion is

$$\frac{d^2 u_0}{dt^2} + \frac{1}{\hbar^2} \left[\epsilon_{k,0}^2 + \frac{4E_k \bar{n}}{3} (\alpha_0 \bar{g}_0 \cos 2\omega_0 t + 2\alpha_2 \bar{g}_2 \cos 2\omega_2 t) \right] u_0 = 0, \quad (35)$$

which is generally a quasiperiodic Mathieu equation. The stability regions in Eq. (35) studied using different approximation methods reveal a very complex structure [60]. When ω_0/ω_2 is a rational number, Eq. (35) exhibits an overall periodicity, and the Floquet theorem becomes valid. Then, the instability regions are just a union of those arising from the independent modulations of a_0 and a_2 . In Fig. 12(a), we show the two primary instability tongues associated with a_0 and a_2 modulations for $\omega_0/\omega_2 = 1/3$ and $\omega_2 = 0.3\omega_z$. The modulation amplitudes are taken such that the peak of $\sigma_0^{(0)}$ and $\sigma_2^{(0)}$ are approximately the same. In the dynamics, we observe an oscillation between the patterns of two different wavelengths $1/k_{u0}^{(0)}$ and $1/k_{u2}^{(0)}$ with $k_{u0}^{(0)} < k_{u2}^{(0)}$ [see Figs. 12(b) and 12(c)].

Similarly, for $\bar{c}_1 \ll \bar{c}_0$, the competing instabilities arise among the two different spin-mode momenta. In that case, the

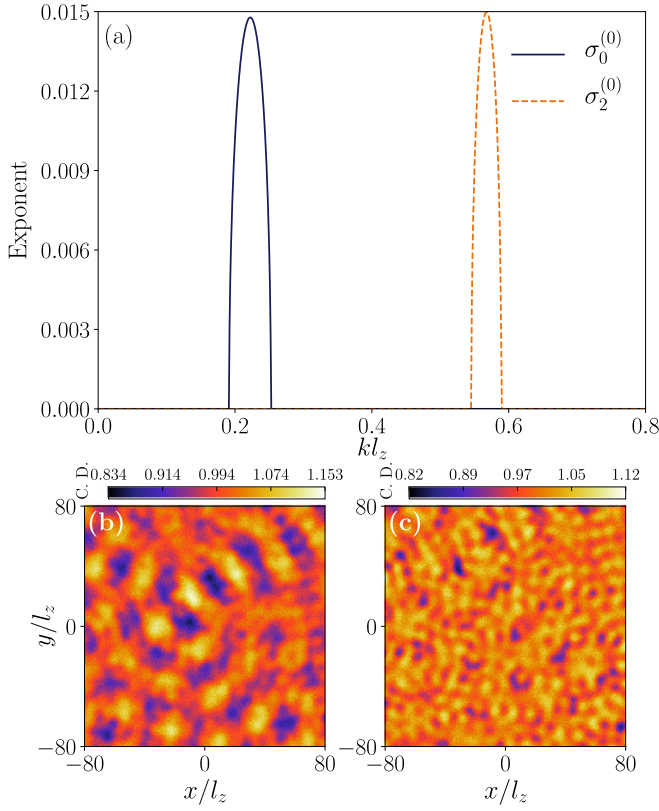


FIG. 12. Competing instabilities among the density modes. (a) The two primary peaks in the Mathieu exponent vs k from the simultaneous modulation of a_0 and a_2 for $\bar{c}_0 \bar{n} = 0.2 \hbar \omega_z$, $\bar{c}_1 \bar{n} = 4 \hbar \omega_z$, $q = 0$, $\alpha_0 = 0.024$, $\omega_0 = 0.1 \omega_z$, $\alpha_2 = 0.01$, and $\omega_2 = 0.3 \omega_z$. The solid line is for a_0 , and the dashed line is for a_2 modulations. (b) and (c) show the density of the $m = 0$ component at $\omega_z t = 420$ and $\omega_z t = 460$, respectively, exhibiting the change in the wavelength of patterns in time. (b) has a wavelength of $1/k_{u0}^{(0)}$, and (c) has a wavelength of $1/k_{u2}^{(0)}$ with $k_{u0}^{(0)} < k_{u2}^{(0)}$.

relevant Mathieu equation is

$$\frac{d^2 u_+}{dt^2} + \frac{1}{\hbar^2} \left[\epsilon_{k, \pm 1}^2 - \frac{4(E_k + q) \bar{n}}{3} \right. \\ \left. \times (\alpha_0 \bar{g}_0 \cos 2\omega_0 t - \alpha_2 \bar{g}_2 \cos 2\omega_2 t) \right] u_+ = 0. \quad (36)$$

Again, for a rational ratio of ω_0/ω_2 , we obtain the instability tongues from the union of instabilities, as shown in Fig. 13(a). The effect of competing instabilities is directly visible in the behavior of the spin-spin correlation functions during the transient stage, and they are of the form

$$C_{x,y}(\rho, t) = D(t) J_0(k_{u0}^{(+)} \rho) + [1 - D(t)] J_0(k_{u2}^{(+)} \rho), \quad (37)$$

$$C_z(\rho, t) = J_0(k_{u0}^{(+)} \rho) J_0(k_{u2}^{(+)} \rho), \quad (38)$$

where $k_{u0}^{(+)}$ and $k_{u2}^{(+)}$ are unstable momenta of the spin mode from modulation frequencies ω_0 and ω_2 and $D(t)$ is the time-dependent amplitude.

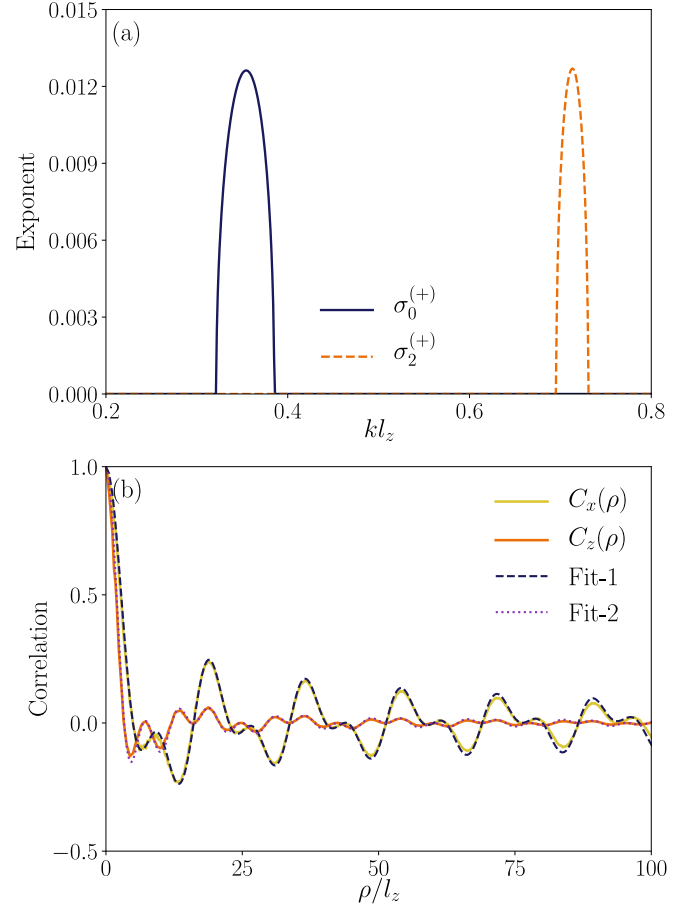


FIG. 13. Competing instabilities among the spin modes. (a) The two primary peaks in the Mathieu exponent vs k from the simultaneous modulation of a_0 and a_2 for $\bar{c}_0 \bar{n} = 0.4 \hbar \omega_z$, $\bar{c}_1 \bar{n} = 0.05 \hbar \omega_z$, $q = 0$, $\alpha_0 = 0.205$, $\omega_0 = 0.1 \omega_z$, $\alpha_2 = 0.1$, and $\omega_2 = 0.3 \omega_z$. The solid line is for a_0 , and the dashed line is for a_2 modulations. (b) shows the spin-spin correlation functions $C_x(\rho)$ and $C_z(\rho)$. Fit-1 and Fit-2 are, respectively, Eqs. (37) and (38). The numerical results in (b) are obtained by taking the average over 10 realizations of noises.

VI. EXPERIMENTAL CONSIDERATIONS

Now, we briefly examine the experimental possibilities. As discussed above, the emergent spin textures leading to PCVs can be observed except when $\bar{c}_0 \ll |\bar{c}_1|$, for which the spin mode is completely outplayed by the density mode in the instability dynamics. In the state-of-the-art experimental setups of spin-1 condensates, for instance, in ^{23}Na , ^{87}Rb , and ^7Li , the ratio \bar{c}_1/\bar{c}_0 is, respectively, 0.036, -0.004 [36], and -0.46 [61], which supports the formation of spin textures and PCVs. For ^{87}Rb and ^7Li , since the spin-dependent interactions are ferromagnetic, preparing the initial polar phase requires a quadratic Zeeman field. We numerically verified all three cases and confirmed the formation of spin textures and PCVs is identical to the case with degenerate modes. In a given atomic setup, Feshbach resonances are required to access the different regimes of interaction strengths we consider, and in particular, independent control of a_0 and a_2 is needed. The latter has been proposed via combining magnetic and rf-field-induced Feshbach resonances [53]. Longitudinal

and transverse spin-spin correlations are computed once the corresponding magnetizations are measured, as demonstrated in Ref. [62].

VII. SUMMARY AND OUTLOOK

In summary, we analyzed the density patterns and spin textures in a parametrically driven Q2D spin-1 condensate for two initial phases: ferromagnetic and polar. An initial ferromagnetic condensate is immune to periodic modulation of a_0 , whereas for a_2 modulation, it exhibits dynamics similar to that of a scalar condensate. An initial polar phase revealed interesting dynamics; for instance, a gas of polar core vortices and antivortices is seen, with its density determined by the momentum of the unstable spin mode. Also, there is competition between Faraday patterns and spin-mixing dynamics which can be controlled by tuning the interaction strengths, quadratic Zeeman field, or driving frequencies. When spin-mixing dynamics dominates, the spin-spin correlation functions exhibit a Bessel function behavior as a function of the relative distance. Otherwise, they decay exponentially with a correlation length of the order of a spin healing length. Modulating both scattering lengths creates an exciting scenario of competing instabilities among density or spin modes. It produces the superposition of Faraday patterns or spin correlation functions of two distinct wavelengths.

Our studies open up several perspectives for future studies. For instance, one could select an appropriate initial state to engineer exotic spin textures or vortices via periodic modulation. The same analyses can be extended to condensates of higher spin in which the availability of three or more scattering lengths may lead to complex scenarios. Another exciting aspect would be to analyze the effect of harmonic confinement and the role of transverse excitations.

ACKNOWLEDGMENTS

We acknowledge C. Mishra for the discussions during the initial stages of the work. We thank the National Supercomputing Mission (NSM) for providing the computing resources of “PARAM Brahma” at IISER Pune, which is implemented by C-DAC and supported by the Ministry of Electronics and Information Technology (MeitY) and Department of Science and Technology (DST), Government of India. R.N. further acknowledges DST-SERB for Swarnajayanti Fellowship File No. SB/SJF/2020-21/19 and a MATRICS grant (Grant No. MTR/2022/000454) from SERB, Government of India, and the National Mission on Interdisciplinary Cyber-Physical Systems (NM-ICPS) of the Department of Science and Technology, Government of India, through the I-HUB Quantum Technology Foundation, Pune, India.

-
- [1] K. Staliunas, S. Longhi, and G. J. de Valcárcel, *Phys. Rev. Lett.* **89**, 210406 (2002).
 - [2] P. Engels, C. Atherton, and M. A. Hofer, *Phys. Rev. Lett.* **98**, 095301 (2007).
 - [3] A. I. Nicolin, R. Carretero-González, and P. G. Kevrekidis, *Phys. Rev. A* **76**, 063609 (2007).
 - [4] R. Nath and L. Santos, *Phys. Rev. A* **81**, 033626 (2010).
 - [5] K. Staliunas, S. Longhi, and G. J. de Valcárcel, *Phys. Rev. A* **70**, 011601(R) (2004).
 - [6] M. Modugno, C. Tozzo, and F. Dalfovo, *Phys. Rev. A* **74**, 061601(R) (2006).
 - [7] N. Katz and O. Agam, *New J. Phys.* **12**, 073020 (2010).
 - [8] A. I. Nicolin, *Phys. Rev. E* **84**, 056202 (2011).
 - [9] P. Capuzzi, M. Gattobigio, and P. Vignolo, *Phys. Rev. A* **83**, 013603 (2011).
 - [10] K. Łakomy, R. Nath, and L. Santos, *Phys. Rev. A* **86**, 023620 (2012).
 - [11] A. Balaž and A. I. Nicolin, *Phys. Rev. A* **85**, 023613 (2012).
 - [12] A. Balaž, R. Paun, A. I. Nicolin, S. Balasubramanian, and R. Ramaswamy, *Phys. Rev. A* **89**, 023609 (2014).
 - [13] B. K. Turmanov, B. B. Baizakov, and F. K. Abdullaev, *Phys. Rev. A* **101**, 053616 (2020).
 - [14] A. B. Bhattacharjee, *Phys. Scr.* **78**, 045009 (2008).
 - [15] J. B. Sudharsan, R. Radha, M. C. Raportaru, A. I. Nicolin, and A. Balaž, *J. Phys. B* **49**, 165303 (2016).
 - [16] R. Cominotti, A. Berti, A. Farolfi, A. Zenesini, G. Lamporesi, I. Carusotto, A. Recati, and G. Ferrari, *Phys. Rev. Lett.* **128**, 210401 (2022).
 - [17] H. Zhang, S. Liu, and Y.-S. Zhang, *Phys. Rev. A* **105**, 063319 (2022).
 - [18] G. Verma, U. D. Rapol, and R. Nath, *Phys. Rev. A* **95**, 043618 (2017).
 - [19] H. Lignier, C. Sias, D. Ciampini, Y. Singh, A. Zenesini, O. Morsch, and E. Arimondo, *Phys. Rev. Lett.* **99**, 220403 (2007).
 - [20] A. Eckardt, T. Jinasundera, C. Weiss, and M. Holthaus, *Phys. Rev. Lett.* **95**, 200401 (2005).
 - [21] A. Zenesini, H. Lignier, D. Ciampini, O. Morsch, and E. Arimondo, *Phys. Rev. Lett.* **102**, 100403 (2009).
 - [22] W. Zhang, B. Sun, M. S. Chapman, and L. You, *Phys. Rev. A* **81**, 033602 (2010).
 - [23] T. M. Hoang, C. S. Gerving, B. J. Land, M. Anquez, C. D. Hamley, and M. S. Chapman, *Phys. Rev. Lett.* **111**, 090403 (2013).
 - [24] L. W. Clark, A. Gaj, L. Feng, and C. Chin, *Nature (London)* **551**, 356 (2017).
 - [25] H. Fu, L. Feng, B. M. Anderson, L. W. Clark, J. Hu, J. W. Andrade, C. Chin, and K. Levin, *Phys. Rev. Lett.* **121**, 243001 (2018).
 - [26] Z. Wu and H. Zhai, *Phys. Rev. A* **99**, 063624 (2019).
 - [27] H. Fu, Z. Zhang, K.-X. Yao, L. Feng, J. Yoo, L. W. Clark, K. Levin, and C. Chin, *Phys. Rev. Lett.* **125**, 183003 (2020).
 - [28] H. Saito and M. Ueda, *Phys. Rev. Lett.* **90**, 040403 (2003).
 - [29] F. K. Abdullaev, J. G. Caputo, R. A. Kraenkel, and B. A. Malomed, *Phys. Rev. A* **67**, 013605 (2003).
 - [30] S. Lellouch, M. Bukov, E. Demler, and N. Goldman, *Phys. Rev. X* **7**, 021015 (2017).
 - [31] J. Bera, A. Q. Batin, S. Ghosh, B. Malomed, and U. Roy, *Philos. Trans. R. Soc., A* **381**, 20220075 (2023).
 - [32] J. H. V. Nguyen, M. C. Tsatsos, D. Luo, A. U. J. Lode, G. D. Telles, V. S. Bagnato, and R. G. Hulet, *Phys. Rev. X* **9**, 011052 (2019).

- [33] Z. Zhang, K.-X. Yao, L. Feng, J. Hu, and C. Chin, *Nat. Phys.* **16**, 652 (2020).
- [34] L. E. Sadler, J. M. Higbie, S. R. Leslie, M. Vengalattore, and D. M. Stamper-Kurn, *Nature (London)* **443**, 312 (2006).
- [35] D. M. Stamper-Kurn and M. Ueda, *Rev. Mod. Phys.* **85**, 1191 (2013).
- [36] Y. Kawaguchi and M. Ueda, *Phys. Rep.* **520**, 253 (2012).
- [37] H. Saito and H. Hyuga, *Phys. Rev. A* **78**, 033605 (2008).
- [38] T. M. Hoang, M. Anquez, B. A. Robbins, X. Y. Yang, B. J. Land, C. D. Hamley, and M. S. Chapman, *Nat. Commun.* **7**, 11233 (2016).
- [39] B. Evrard, A. Qu, K. Jiménez-García, J. Dalibard, and F. Gerbier, *Phys. Rev. A* **100**, 023604 (2019).
- [40] Y. Imaeda, K. Fujimoto, and Y. Kawaguchi, *Phys. Rev. Res.* **3**, 043090 (2021).
- [41] P. Xu and W. Zhang, *Phys. Rev. A* **104**, 023324 (2021).
- [42] S. Dadras, A. Gresch, C. Groiseau, S. Wimberger, and G. S. Summy, *Phys. Rev. Lett.* **121**, 070402 (2018).
- [43] S. Dadras, A. Gresch, C. Groiseau, S. Wimberger, and G. S. Summy, *Phys. Rev. A* **99**, 043617 (2019).
- [44] K. Sah, Faraday patterns in spinor spin-1 Bose-Einstein condensates, MS thesis, Indian Institute of Science Education and Research Pune, 2019.
- [45] H. Saito, Y. Kawaguchi, and M. Ueda, *Phys. Rev. A* **76**, 043613 (2007).
- [46] L. A. Williamson and P. B. Blakie, *Phys. Rev. Lett.* **116**, 025301 (2016).
- [47] K. Kumar and K. M. S. Bajaj, *Phys. Rev. E* **52**, R4606(R) (1995).
- [48] C. Chin, R. Grimm, P. Julienne, and E. Tiesinga, *Rev. Mod. Phys.* **82**, 1225 (2010).
- [49] T. V. Tscherbul, T. Calarco, I. Lesanovsky, R. V. Krems, A. Dalgarno, and J. Schmiedmayer, *Phys. Rev. A* **81**, 050701(R) (2010).
- [50] Y. Ding, J. P. D’Incao, and C. H. Greene, *Phys. Rev. A* **95**, 022709 (2017).
- [51] T. M. Hanna, E. Tiesinga, and P. S. Julienne, *New J. Phys.* **12**, 083031 (2010).
- [52] D. J. Papoular, G. V. Shlyapnikov, and J. Dalibard, *Phys. Rev. A* **81**, 041603(R) (2010).
- [53] P. Zhang, P. Naidon, and M. Ueda, *Phys. Rev. Lett.* **103**, 133202 (2009).
- [54] T. Boulier, J. Maslek, M. Bukov, C. Bracamontes, E. Magnan, S. Lellouch, E. Demler, N. Goldman, and J. V. Porto, *Phys. Rev. X* **9**, 011047 (2019).
- [55] P. Zhang and Y. Gu, *SciPost Phys.* **9**, 079 (2020).
- [56] R. Barnett, A. Polkovnikov, and M. Vengalattore, *Phys. Rev. A* **84**, 023606 (2011).
- [57] T. Isoshima, K. Machida, and T. Ohmi, *J. Phys. Soc. Jpn.* **70**, 1604 (2001).
- [58] T. Mizushima, N. Kobayashi, and K. Machida, *Phys. Rev. A* **70**, 043613 (2004).
- [59] A. Lamacraft, *Phys. Rev. Lett.* **98**, 160404 (2007).
- [60] I. Kovacic, R. Rand, and S. Mohamed Sah, *Appl. Mech. Rev.* **70**, 020802 (2018).
- [61] S. J. Huh, K. Kim, K. Kwon, and J.-Y. Choi, *Phys. Rev. Res.* **2**, 033471 (2020).
- [62] S. Huh, K. Mukherjee, K. Kwon, J. Seo, S. I. Mistakidis, H. R. Sadeghpour, and J. Choi, [arXiv:2303.05230](https://arxiv.org/abs/2303.05230).

Correction: Equation (1) contained an error and has been fixed.